

Received 5 January 2024, accepted 25 January 2024, date of publication 13 February 2024, date of current version 1 March 2024.

Digital Object Identifier 10.1109/ACCESS.2024.3365541

## RESEARCH ARTICLE

# High-Precision Modeling for Arbitrary Curved Frequency Selective Structures Based on Perfect Mapping Between Thick Surface and Its Minimum Distortion Flat-Unfolding Solution

HUANG MINJIE 

School of Aeronautic Science and Engineering, Beihang University, Beijing 100191, China

e-mail: huangminjie@buaa.edu.cn


This work was supported by the National Natural Science Foundation of China under Grant 61601015.

**ABSTRACT** How to arrange a periodic array consisting of precise unit-cells on a complex surface has always been a difficulty affecting the application of frequency selective structures. Based on the elastic deformation theory of thin-shell, a perfect mapping between a curved surface and a planar array by using the weighted minimum distortion flat-unfolding solution of the surface is established and then extended to the 3-Dimensional (3D) case along the thickness direction. With the help of this mapping, the information of the unit-cell can be mapped to the thick surface structure while maintaining the topological properties of the planar periodic array and the internal structure of the unit-cell. In the mapping process, the deformation of the unit-cell on the thick surface structure relative to the original unit-cell can be evaluated, and this deformation has local adjustability. This manuscript provides a class of local unit-cell deformation control algorithms that do not affect the completeness of the mapping. The application effect and potential of this method are demonstrated by an example of a spliced conical radome using a three-layer hybrid unit-cell.

**INDEX TERMS** Frequency selective surface (FSS), radome, electromagnetic functional structure, flat unfolding, thin-shell, elastic deformation, perfect mapping.

## I. INTRODUCTION

Components that integrate the characteristics of stealth shape, electromagnetic wave absorption or emission, frequency selection or metamaterials, and undertake certain structural functions, have been an important development direction in the fields of low detectability, electromagnetic compatibility, and high-performance communication technology. This type of structure is an extension of the traditional concepts of frequency selective surfaces (FSSs) and metasurfaces but focuses more on applications and is commonly referred to

The associate editor coordinating the review of this manuscript and approving it for publication was Shah Nawaz Burokur .

as “electromagnetic functional structures” or “artificial electromagnetic structures” [1], [2]. At present, great progress has been made in the field of absorbing/scattering frequency selective surfaces (AFSS/SFSS), ultra-wideband frequency selective surfaces (UWB-FSS), non-resonant frequency selective surfaces (NR-FSS) and metamaterials. In terms of function, the unit-cell of electromagnetic functional structure has developed towards multi-frequency, integrated absorption and scattering, broadband/ultra-wideband, negative refractive index, adjustable performance, etc. In terms of scale, the unit-cell has developed towards a thinner, smaller, and finer structure. However, most of the existing research focuses on the performance of the periodic unit-cell based on the

assumptions of infinity and planarity. Practical electromagnetic functional structural products are mostly curved surfaces, and their applications face many difficulties. Among them, the difficulty of design and modeling is the primary problem that restricts the application of advanced electromagnetic functional structures in components such as curved radomes, non-planar antennas, and smart skins. Without solving the problem of modeling, it is difficult to describe the design schemes and manufacture the prototype samples of those curved electromagnetic functional structures, and it is also difficult to evaluate their electromagnetic performance by accurate computational electromagnetics method.

At the early stage of the development of frequency selection surfaces, many scholars have discussed the problem of how to arrange periodic arrays on curved structures [3], [4], [5]. Traditional research often focuses on relatively simple situations. The applied object is a plane or a developable surface. One can directly arrange unit-cells on the plane first and then map them to the surface [6]. Later, some surfaces with smaller Gaussian curvature were approximated by the developable surface, and arrays were arranged on the developable surface and projected onto the original surface, while the size of the unit-cells was adjusted to correct errors caused by the approximation and projection [7]. For complex surfaces, people have developed a modeling method of local planar approximation, which usually divides complex surfaces into pieces with small Gaussian curvature and arranges arrays by projecting them from the tangent plane onto the pieces [8], [9], [10], [11]. The equal density method and the equal Geodesic method are also two commonly used curved array modeling methods, which inherit the features of periodic arrays on the plane of complex surfaces by maintaining the density of unit-cell [12] and the surface spacing between unit-cells consistent with the plane arrays [13], respectively [14], [15], [16], [17], [18]. These methods, when used alone, usually bring about problems such as drastic changes in the relative position relationship of the unit-cells. Therefore, several curved array modeling methods that combine multiple methods have been developed [17], [18]. Because the algorithmic process is not rigorous, such methods usually come at the cost of some properties of unit-cells or arrays, resulting in only handling some sparse arrays or simple unit-cells. They are generally powerless to deal with advanced FSS structures with features such as compact array, 3D/quasi 3D, or hyperfine unit-cell.

The principle of another kind of curved array structure modeling method is similar to the approximate developable surface method for processing surfaces with small Gaussian curvature. It is based on the direct approximate flat-unfolding plane of the surface, by arranging unit-cells on the approximate flat-unfolding plane and then mapping back to the surface [19], [20], [21]. However, perhaps due to various reasons such as not all surfaces having small distortion flat-unfolding planes, uncontrollable distortion rates at different positions, and the high cost of solving the flat-unfolding

solutions of large surfaces, there are few studies on the design of arbitrary curved array structures by these methods. On the other hand, in the field of surface texture, clothing design, stamping and other fields where the requirements for flattening distortion are not strict, such methods are widely used [22], [23], [24], [25], [26]. Surface texture and clothing design are not sensitive to local shape scaling or distortion, while clothing design allows splicing and assumes that the material is plastic. Stamping pays more attention to the accuracy of overall deformation and appearance, while the importance of local deformation is very low. Map surveying only focuses on very special surfaces such as spheres, and its focus differs greatly from the structure of curved radomes. Therefore, these methods cannot be directly used for high-precision curved array structure design.

Overall, the method based on the minimum distortion flat-unfolding solution of surfaces has natural advantages in maintaining the topological characteristics and fine features of the unit-cell and array. Considering these, the manuscript aims to establish a high-precision modeling method for curved arrays with complex fine unit-cell by constructing a perfect mapping between an arbitrary thick surface structure and a thick flat plate. The main content is divided into three parts. Section II introduces a method for solving the minimum distortion flat-unfolding problem of an arbitrary surface with adjustable local distortion. In Section III, the surface and its minimum distortion flat-unfolding solution are extended along the thickness direction to construct a perfect mapping between the thick curved structure and the thick flat plate; If this mapping relationship is viewed as a deformation process, the deformation maintains the characteristic of minimum distortion. Section IV demonstrates the effectiveness of this method through a modeling example of an FSS radome with a tight array of multi-layer aperture-patch hybrid unit-cells; Then the electromagnetic performance simulation of the modeling results by FEKO software shows the potential of the method to provide a computational model for large complex curved FSSs.

## II. A METHOD OF PERIODIC ARRAY ARRANGEMENT ON CURVED SURFACE BASED ON THE MINIMUM ELASTIC DEFORMATION OF THIN-SHELL

If a surface can be unfolded to plane according to a certain minimum deformation rule, a mapping relationship between the points on the surface and points on the plane can be established. The periodic array can be arranged on the plane first, and then the geometric information of the planar periodic array can be mapped back to the original surface to complete the arrangement of the periodic array on the surface (Fig. 1). This method attempts to maintain the topological relationship between the unit-cells to the maximum extent through a perfect mapping of global deformation and weakens the deformation of the curved array relative to the planar periodic array by minimizing the flat-unfolding distortion. Therefore,

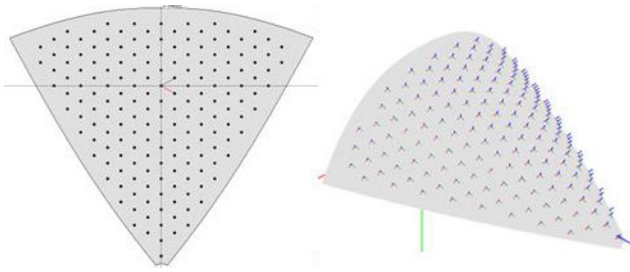


**FIGURE 1.** The concept of the array arrangement based on the minimum distortion flat-unfolding plane of curved surface.

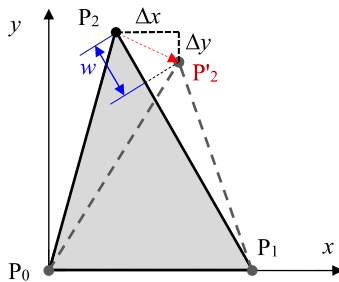


**FIGURE 2.** Deformation caused by the length change of one side of a triangle.

the key to the method is to solve the minimum distortion flat-unfolding solution of the surface.

**A. DEFINITION OF THE MINIMUM DISTORTION**

Firstly, a reasonable definition of “minimum distortion” is needed. Fig. 2 shows a triangular sheet  $\Delta P_0P_1P_2$  with elastic modulus  $E$  and Poisson’s ratio  $\mu$ . We define a local plane coordinate system with the origin at vertex  $P_0$  and the x-axis along edge  $\overrightarrow{P_0P_1}$ . In this coordinate system, assume the coordinates of  $P_1$  and  $P_2$  to be  $(x_1, 0)$  and  $(x_2, y_2)$  respectively, and assume the three sides of  $\Delta P_0P_1P_2$  to be:

$$\begin{cases} \vec{l}_0 = \overrightarrow{P_1P_2} \\ \vec{l}_1 = \overrightarrow{P_2P_0} \\ \vec{l}_2 = \overrightarrow{P_0P_1} \end{cases} \quad (1)$$

When the length of side  $\vec{l}_0$  increases by  $w$  and the lengths of other sides remain unchanged, the position of  $P_2$  will change. If the position of  $P_2$  changes to  $P'_2(x', y') = (x_2 + \Delta x, y_2 + \Delta y)$ , the coordinate of  $P'_2$  should meet the following equations:

$$\begin{cases} x'^2 + y'^2 = x_2^2 + y_2^2 \\ w = \sqrt{(x' - x_1)^2 + y'^2} - \sqrt{(x_2 - x_1)^2 + y_2^2} \end{cases} \quad (2)$$

The displacement and corresponding deformation in the  $x$  and  $y$  directions of any point  $(x, y)$  in  $\Delta P_0P_1P_2$  caused by  $w$  can be expressed as:

$$\begin{bmatrix} u \\ v \end{bmatrix} = \begin{bmatrix} \Delta x \\ \Delta y \end{bmatrix} - \frac{1}{y_2} \begin{bmatrix} 0 & -\Delta x \\ 0 & -\Delta y \end{bmatrix} \left( \begin{bmatrix} x \\ y \end{bmatrix} - \begin{bmatrix} x_2 \\ y_2 \end{bmatrix} \right) \quad (3)$$

$$\begin{bmatrix} \partial u / \partial x & \partial u / \partial y \\ \partial v / \partial x & \partial v / \partial y \end{bmatrix} = \frac{1}{y_2} \begin{bmatrix} 0 & \Delta x \\ 0 & \Delta y \end{bmatrix} \quad (4)$$

Therefore, the strains at point  $(x, y)$  are obtained [27]:

$$\begin{cases} \epsilon_x = \partial u / \partial x = 0 \\ \epsilon_y = \partial v / \partial y = \Delta y / y_2 \\ \gamma_{xy} = \partial v / \partial x + \partial u / \partial y = \Delta x / y_2 \end{cases} \quad (5)$$

The expressions in (5) do not contain the coordinate components  $x$  and  $y$ , which indicates that they describe a constant strain field. Since the thickness is not considered, the relationship between stress and strain under the plane strain conditions can be used [27]:

$$\begin{bmatrix} \epsilon_x \\ \epsilon_y \\ \gamma_{xy} \end{bmatrix} = \frac{1}{E} \begin{bmatrix} 1 - \mu^2 & -(1 + \mu)\mu & 0 \\ -(1 + \mu)\mu & 1 - \mu^2 & 0 \\ 0 & 0 & 2(1 + \mu) \end{bmatrix} \times \begin{bmatrix} \sigma_x \\ \sigma_y \\ \tau_{xy} \end{bmatrix} \quad (6)$$

$$\begin{bmatrix} \sigma_x \\ \sigma_y \\ \tau_{xy} \end{bmatrix} = \frac{E}{(2\mu - 1)(\mu + 1)} \begin{bmatrix} \mu - 1 & -\mu & 0 \\ -\mu & \mu - 1 & 0 \\ 0 & 0 & (2\mu - 1)/2 \end{bmatrix} \times \begin{bmatrix} \epsilon_x \\ \epsilon_y \\ \gamma_{xy} \end{bmatrix} \quad (7)$$

If  $w$  has a tinny change  $\delta w$ , the stress work per unit volume can be described as:

$$\begin{aligned} \delta W &= \sigma_x \frac{d}{dw} \left( \frac{\partial u}{\partial x} \right) \delta w + \sigma_y \frac{d}{dw} \left( \frac{\partial v}{\partial y} \right) \delta w \\ &\quad + \tau_{xy} \frac{d}{dw} \left( \frac{\partial v}{\partial x} + \frac{\partial u}{\partial y} \right) \delta w \\ &= \frac{1}{y_2} \left( \sigma_y \frac{d\Delta y}{dw} \delta w + \tau_{xy} \frac{d\Delta x}{dw} \delta w \right) \end{aligned} \quad (8)$$

By solving (2), the expressions of the following variables are obtained:

$$\begin{cases} x' = \left[ l_1^2 + l_2^2 - (w + l_0)^2 \right] / (2l_2) \\ y' = \sqrt{l_1^2 - x'^2} \end{cases} \quad (9)$$

$$\begin{cases} \Delta x = \left[ l_1^2 + l_2^2 - (w + l_0)^2 \right] / (2l_2) - x_2 \\ \Delta y = \sqrt{l_1^2 - x'^2} - y_2 \end{cases} \quad (10)$$

$$\begin{cases} \frac{d\Delta x}{dw} = -\frac{w + l_0}{l_2} \\ \frac{d\Delta y}{dw} = \frac{l_2}{\sqrt{l_1^2 - x'^2}} \frac{w + l_0}{l_2} \end{cases} \quad (11)$$

where  $l_i$  is the length of  $\vec{l}_i$ . Substitute (9)-(11) into (8) to obtain:

$$\delta W = \frac{E(w + l_0)}{y_2^2 l_2 (1 + \mu)} \left( \frac{\mu - 1}{2\mu - 1} \frac{x' \Delta y}{\sqrt{l_1^2 - x'^2}} - \frac{\Delta x}{2} \right) \delta w \quad (12)$$

If the length of side  $\vec{l}_0$  changes significantly by  $\Delta l$ , the volume density of internal stress work is the integral of  $\delta W$ :

$$W = \int_0^{\Delta l} \frac{E(w+l_0)}{y_2^2 l_2 (1+\mu)} \left( \frac{\mu-1}{2\mu-1} \frac{x' \Delta y}{\sqrt{l_1^2 - x'^2}} - \frac{\Delta x}{2} \right) dw \quad (13)$$

If  $\Delta l \ll l_1$  or using the small deformation approximation, we can use

$$x_2 \Delta x + y_2 \Delta y = 0 \quad (14)$$

to replace the first equation in (2), which means point  $P_2'$  on the circle with a radius of  $l_2$  is approximately replaced by the point on the tangent line of the circle. In this way, the volume density of internal stress work is simplified to an explicit expression:

$$W = \frac{E}{(1+\mu)} \left( \frac{l_0}{x_1 y_2} \right)^2 \left( \frac{\mu-1}{2\mu-1} \frac{x_2^2}{y_2^2} + \frac{1}{2} \right) \frac{\Delta l^2}{2} \quad (15)$$

The strain energy  $E_S$  of  $\Delta P_0 P_1 P_2$  caused by  $\Delta l$  is the volume integral of the stress work density:

$$E_S(\Delta P_0 P_1 P_2, \Delta l) = SW \quad (16)$$

where  $S$  is the area of  $\Delta P_0 P_1 P_2$ .

Expression (16) is the strain energy caused by the length change of side  $\vec{l}_0$  only. If any side changes, the corresponding strain energy expression can be obtained by changing the subscripts of the parameters in (13) or (15). When the length of side  $\vec{l}_i$  increases by  $w_i$ , take (15) as an example, the resulting stress work density can be written as:

$$W_i = \frac{E}{(1+\mu)} \left( \frac{l_i}{x_{i,1} y_{i,2}} \right)^2 \left( \frac{\mu-1}{2\mu-1} \frac{x_{i,2}^2}{y_{i,2}^2} + \frac{1}{2} \right) \frac{w_i^2}{2} \quad (17)$$

where

$$x_{i,1} = l_{i+2} \quad (18)$$

$$x_{i,2} = -\vec{l}_{i+1} \cdot \hat{l}_{i+2} \quad (19)$$

$$y_{i,2} = \vec{l}_i \cdot (\hat{n} \times \vec{l}_{i+2}) / |\hat{n} \times \vec{l}_{i+2}| \quad (20)$$

$$\hat{n} = (\vec{l}_i \times \vec{l}_{i+1}) / |\vec{l}_i \times \vec{l}_{i+1}| \quad (21)$$

For the convenience of expressing, the subscript “ $i+m$ ” of all parameters should be understood as  $\text{mod}(i+m, 3)$ , which means  $l_{i+3} = l_i$ .

When the lengths of all three sides of  $\Delta P_0 P_1 P_2$  change, the strain energy can be approximately expressed as the sum of the strain energy generated by the deformation of each side, as follows:

$$E_T = S \sum_{i=0}^2 W_i \quad (22)$$

The strain energy  $E_T$  is a function of  $W_i (i = 0, 1, 2)$ .

In the next discussion, we define the space coordinate of vertex  $P_i$  of  $\Delta P_0 P_1 P_2$  as  $(x_i, y_i, z_i)$ , and define planar triangle  $\Delta V_0 V_1 V_2$  as a deformed image of  $\Delta P_0 P_1 P_2$ . Assuming the

coordinate of vertex  $V_i$  of  $\Delta V_0 V_1 V_2$  is  $V_i(u_i, v_i)$ , then the lengths of the three sides of  $\Delta V_0 V_1 V_2$  are given as:

$$d_i = \sqrt{(u_{i+2} - u_{i+1})^2 + (v_{i+2} - v_{i+1})^2} \quad (23)$$

The side lengths before flattening are

$$l_i = \sqrt{(x_{i+2} - x_{i+1})^2 + (y_{i+2} - y_{i+1})^2 + (z_{i+2} - z_{i+1})^2} \quad (24)$$

Then the side-length change before and after deformation  $w_i = d_i - l_i$  is a function of  $(u_i, v_i) (i = 0, 1, 2)$ .

Since  $E_T$  is used to measure the distortion degree of  $\Delta P_0 P_1 P_2$  when it is deformed,  $E_T = 0$  if and only if  $w_i = 0 (i = 0, 1, 2)$ .

Any complex surface can be approximated by triangular facets. Suppose that surface  $S$  is discretized into a discrete surface  $S'$  composed of  $M$  triangular facets and  $N$  vertices, and the vertex coordinate set of  $S'$  is:

$$\mathbf{P} = \{P_i | i = 0, 1, 2, \dots, N-1\} \quad (25)$$

Suppose a flat-unfolding solution of the discrete surface  $S'$  is plane  $F'$ , and the vertex coordinate set corresponding to  $\mathbf{P}$  on  $F'$  is

$$\mathbf{V} = \{V_i | i = 0, 1, 2, \dots, N-1\} \quad (26)$$

where,  $F'$  is actually a continuous region composed of triangles on a 2D plane. If  $E_{T,j} = S_j \sum_{i=0}^2 W_{j,i}$  is used to represent the strain energy of the  $j$ -th triangular facet  $\Delta_j$  on the discrete surface  $S'$  when  $S'$  is unfolded to  $F'$ , the total strain energy can be expressed as the sum of the strain energy caused by the deformation of each triangular facet:

$$U = \sum_{j=0}^{M-1} t_j E_{T,j} = \sum_{j=0}^{M-1} (t_j S_j \sum_{i=0}^2 W_{j,i}) \quad (27)$$

where the definition of  $W_{j,i}$  is like (17), which represents the strain energy caused by the deformation of the  $i$ -th edge of triangular facet  $\Delta_j$  on the discrete surface  $S'$ , and  $S_j$  is the area of  $\Delta_j$ .  $t_j$  is the weight coefficient of the proportion of strain energy of  $\Delta_j$  in the total strain energy, which also can be understood as the thickness of  $\Delta_j$ .

In this paper, the total strain energy  $U$  is selected to measure the distortion degree of  $S'$  when flattened to  $F'$ , and the “minimum distortion” is the minimum value of  $U$ . If thickness of all triangular facets is the same or not considered, then  $t_j = 1$ . Otherwise, a larger  $t_j$  means that the distortion of facet  $\Delta_j$  has a greater impact on  $U$ , and the distortion of facet  $\Delta_j$  will be weakened in the process of flattening solution.

## B. SOLVING OF THE MINIMUM DISTORTION FLAT-UNFOLDING PROBLEM

The standard form of the minimum value problem of can be described as follows:

$$\begin{cases} \mathbf{V} = \{V_i(u_i, v_i) | i = 0, 1, 2, \dots, N-1\} \\ \min U(\mathbf{V}) \end{cases} \quad (28)$$

This is a multivariable unconstrained optimization problem. There are many algorithms to solve problem (28), such as gradient method, Newton iterative method, simplex method and so on. However, for arbitrary surface, no matter which optimization method is used, the solution search process may converge to a local optimal solution, especially the unfolding solution with overlapping of triangle facets, rather than the global optimal solution. It is easy to understand physically that the strain energy of an unfolding solution with “wrinkles” is probably smaller than that of a solution without “wrinkles”. Therefore, when using these algorithms in practice, the flat-unfolding process can be guided by artificially introducing some intermediate solutions to avoid “wrinkles”. Those intermediate unfolding solutions are similar to the multi-stage “molds” in the metal sheet stamping process. This is an interesting research direction.

### C. ARRANGEMENT OF THE PERIODIC ARRAY

After obtaining the minimum distortion flat-unfolding solution of a surface, we can easily determine the geometric features of the periodic array on the unfolding plane, and then map them to the original surface. Since all geometric features are based on points, determining the relationship between the points on the surface and the points on its minimum distortion unfolding plane establishes a mapping between the array on the surface and the array on the minimum unfolding plane.

Let  $M$  is a point on  $\Delta V_i V_j V_k$  of the flat-unfolding solution  $F'$ , and the image of  $\Delta V_i V_j V_k$  on the original surface is  $\Delta P_i P_j P_k$ . Point  $M$  can be expressed as a linear form about the vertices of  $\Delta V_i V_j V_k$ , such as:

$$\vec{M} = \alpha \vec{V}_i + \beta \vec{V}_j + (1 - \alpha - \beta) \vec{V}_k \quad (29)$$

where

$$\begin{aligned} \alpha &= \frac{[\hat{n} \times (\vec{V}_j - \vec{V}_k)] \cdot (\vec{M} - \vec{V}_k)}{[\hat{n} \times (\vec{V}_j - \vec{V}_k)] \cdot (\vec{V}_i - \vec{V}_k)} \\ \beta &= \frac{[\hat{n} \times (\vec{V}_i - \vec{V}_k)] \cdot (\vec{M} - \vec{V}_k)}{[\hat{n} \times (\vec{V}_i - \vec{V}_k)] \cdot (\vec{V}_j - \vec{V}_k)} \end{aligned} \quad (30)$$

and  $\hat{n}$  is the normal direction of  $\Delta V_i V_j V_k$ . Then the image of point  $M$  on the original surface can be expressed as

$$\vec{T} = \alpha \vec{P}_i + \beta \vec{P}_j + (1 - \alpha - \beta) \vec{P}_k \quad (31)$$

The formulas (29)~(31) actually establish a perfect mapping between the minimum distortion flat-unfolding solution  $F'$  and the discrete surface  $S'$ . If we arrange a periodic array on  $F'$ , the geometric information can be completely mapped to the discrete surface  $S'$ .

### III. THE ARRANGEMENT PROBLEMS OF MULTILAYER UNIT-CELLS AND 3D UNIT-CELLS

Since simple single-layer unit-cells have less practical value, the current practical unit-cells are usually multi-layer or 3D structures. When multi-layer unit-cells are arranged on a curved surface, there are not only distortion problems caused

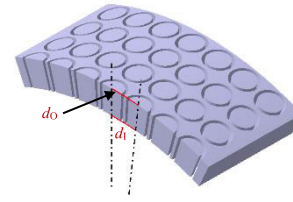


FIGURE 3. The inside and outside distances between the unit-cells are different due to the curvature.

by curvature, but also distortion problems caused by layer alignment and thickness. The distortion caused by layer alignment and thickness can be explained by Fig.3, they usually appear at least one.

If the normal alignment between layers (one of the alignment methods) is guaranteed, the tangential distances between unit-cells on different layer will inevitably change due to the curvature (Fig. 3):  $d_0 > d_1$ . On the other hand, if the tangential distances between the neighbor unit-cells is kept constant, it is theoretically impossible to ensure that elements on different layers are all aligned because the area of each layer surface is different, which will lead to different numbers of unit-cells that can be arranged on different layers.

Due to the design and manufacture difficulties of multi-layer unit-cells or 3D unit-cells, there is few research conclusions on which alignment method is adopted, or whether to keep the array alignment or keep the tangential size of unit-cells on each layer as equal as possible. In this paper, a multi-layer unit-cell placement method that maintains the normal alignment between layers is present. In this method, the geometric information of different layers of the unit-cells is allowed to change with the curvature. The core of this method is to extend the 2D perfect mapping between the unfolding plane and the surface to a 3D perfect mapping between the thick plate and the thick surface by the thickness direction or normal direction extension. The first step is to determine a reference surface of the thick surface structure for flat unfolding.

#### A. DETERMINATION OF THE REFERENCE SURFACE FOR FLAT-UNFOLDING

Because the bending will cause area difference between the two sides of a thick board, it will inevitably lead to the problem that the inner side of the unit-cell becomes narrower, and the outer side becomes wider. In order to minimize the effect of bending on all unit-cells, the problem of determining a flat-unfolding reference surface is introduced. From a geometry perspective, there is usually a neutral surface with no or little deform when bending a plate. To make the 3D geometric feature distortion of a unit-cell as small as possible, the neutral surface or approximate neutral surface is suitable for the flat-unfolding reference surface. That is, the “mid-surface” between the two sides of a thick structure (Fig.4(a) and 4(b)) or the array layer near the “mid-surface” (Fig.4(c)) can be selected as the flat-unfolding reference surface. This

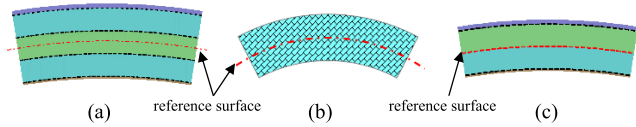


**FIGURE 4.** Selection of the flat-unfolding reference surface. Choose the “mid-surface” of a multi-layer array (a) or a 3D unit-cell array (b), or the array layer near the “mid-surface” of an asymmetric multi-layer array (c) as the flat-unfolding reference surface.

selection can ensure that the distortion of the flat-unfolding reference surface is close to the minimum, while the absolute values of the distortion index of the inner and outer surfaces are approximately equal, but the signs are opposite.

**B. ARRANGEMENT OF MULTI-LAYER UNIT-CELLS ON CURVED SURFACE**

The arrangement of multi-layer array that maintains the normal alignment between layers is essentially to establish a mapping from planar multi-layer unit-cells to the thick structure. This work can be conducted by extending the 2D mapping in Section II to the 3D case along the normal direction of the reference surface. The basic steps are as follows:

(I) Discretize a planar period of the unit-cell into 2D triangle facets.

(II) Any point T in the unit-cell can be expressed in the sum of normal coordinate and tangential coordinates, similar to (29). Assuming that the normal coordinate of point M is t, and the normal projection Q of point M falls on ΔV<sub>i</sub>V<sub>j</sub>V<sub>k</sub> of the discrete model of the planar period, then point M can be written as:

$$\vec{M} = t\hat{z} + \alpha\vec{V}_i + \beta\vec{V}_j + (1 - \alpha - \beta)\vec{V}_k \quad (32)$$

(III) Establish the normal information of the reference surface. Define the normal direction of any vertex on the discrete facet model of a surface as the area-weighted average of the normal directions of all triangular facets sharing the vertex. The normal direction of any point in a triangular facet is a linear sum of the vertex normal directions of the triangle. If point X can be represented by the three vertices of ΔP<sub>i</sub>P<sub>j</sub>P<sub>k</sub> as (29), these definitions can be described as:

$$\vec{n}(P_i) = \frac{\sum_{j \in G_{Fi}} (s_j \hat{n}_j)}{\sum_{j \in G_{Fi}} s_j} \quad (33)$$

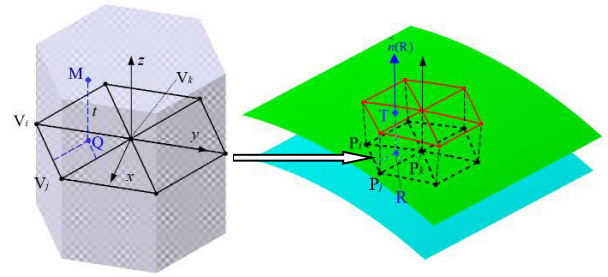
$$\hat{n}(P_i) = \vec{n}(P_i) / |\vec{n}(P_i)| \quad (34)$$

$$\vec{n}(X) = \alpha\hat{n}(P_i) + \beta\hat{n}(P_j) + (1 - \alpha - \beta)\hat{n}(P_k) \quad (35)$$

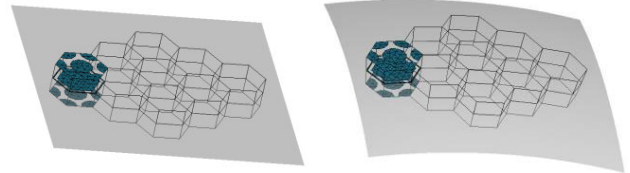
$$\hat{n}(X) = \vec{n}(X) / |\vec{n}(X)| \quad (36)$$

where G<sub>Fi</sub> denotes the serial number set of all facets sharing vertex P<sub>i</sub>, s<sub>j</sub> and  $\hat{n}_j$  denote the area and the normal direction of the j-th facet respectively, and  $\hat{n}(X)$  represents the normal direction at point X.

(IV) After completing the array arrangement on the unfolding plane, triangle facets of the planar period of every unit-cell can be mapped to the reference surface according to the 2D mapping in Section II. Let the image of ΔV<sub>i</sub>V<sub>j</sub>V<sub>k</sub> on the



(a) A unit-cell mapping from plane to surface



(b) An array mapping from plane to surface

**FIGURE 5.** Geometry mapping that maintains the normal alignment between layers.

original surface be ΔP<sub>i</sub>P<sub>j</sub>P<sub>k</sub>, then the image T of point M on the thick surface structure can be expressed as:

$$\vec{T} = t\hat{n}(R) + \alpha\vec{P}_i + \beta\vec{P}_j + (1 - \alpha - \beta)\vec{P}_k \quad (37)$$

where point R is the imagine of Q on ΔP<sub>i</sub>P<sub>j</sub>P<sub>k</sub>.

$$\vec{R} = \alpha\vec{P}_i + \beta\vec{P}_j + (1 - \alpha - \beta)\vec{P}_k \quad (38)$$

Fig. 5 shows an example of a unit-cell whose planar period is a regular hexagon. The above steps can be understood as a process of determining the coordinates of points in sequence: M → Q → R → T. Since point M can be any point in a 3D unit-cell of the planar array, the above steps establish a perfect mapping between the planar array and the thick surface structure. Theoretically, any fine topological structure inside a planar array can be preserved under this mapping.

**C. GEOMETRY ADJUSTMENT OF LOCAL UNIT-CELLS**

In the actual modeling process, it is often necessary to adjust the shape or position of unit-cells in a certain region due to electrical performance adjustments or other performance requirements. Therefore, it is necessary to construct a local geometric structure reconstruction algorithm, which will not destroy the integrity of the whole mapping, but also can be limited to a certain region. In the following, the reconstruction algorithms of several typical geometric deformations in the region with the center point  $\vec{C}$  as the center and the radius R are given. Other local geometric deformations can be designed according to similar methods:

(I) Position adjustment. Assuming that there is a maximum offset  $\vec{d}_{max}$  at point  $\vec{C}$ , the farther the distance from point  $\vec{C}$  is, the smaller the offset is. When the distance from point  $\vec{C}$  is greater than the radius r, the point will not be affected. When this deformation is used to adjust the center position of a unit-cell, it causes the position of other unit-cells around it

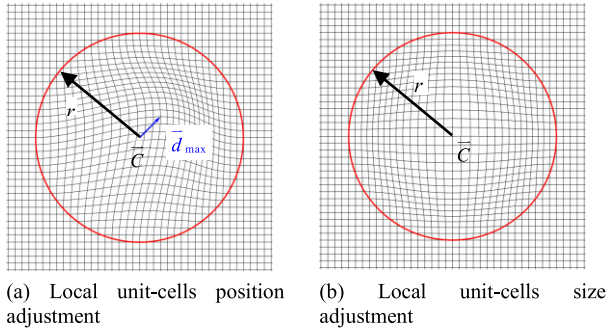


FIGURE 6. The adjustment of the unit-cells in a circular region.

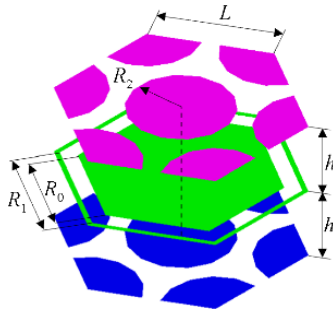


FIGURE 7. A three-layer patch-aperture hybrid unit-cell.

to shift, accompanied by slight tension or compression. The new coordinate  $\vec{M}'$  of point  $\vec{M}$  on the planar array is:

$$\vec{M}' = \begin{cases} \vec{M} + f(|\vec{M} - \vec{C}|/r)\vec{d}_{\max} & |\vec{M} - \vec{C}| < r \\ \vec{M} & |\vec{M} - \vec{C}| \geq r \end{cases} \quad (39)$$

where  $f(x)$  is a continuous function with domain  $[1, 0]$ ,  $f(0) = 1$  and  $f(1) = 0$ . As long as  $r > |\vec{d}|$  is guaranteed, the mapping is still perfect in the circular region.

(II) Size adjustment. It is assumed that the maximum tensile rate of the unit-cell at the center point  $\vec{C}$  is  $\epsilon_{\max}$ , and the tensile rate away from  $\vec{C}$  gradually decreases to 0. When this deformation is used to adjust the size of a unit-cell, it will cause tension or compression of other unit-cells around, accompanied by a slight change in position. The new coordinate  $\vec{M}'$  of point  $\vec{M}$  on the planar array is:

$$\vec{M}' = \begin{cases} \vec{M} + (\vec{M} - \vec{C})f(|\vec{M} - \vec{C}|/r)\epsilon_{\max} & |\vec{M} - \vec{C}| < r \\ \vec{M} & |\vec{M} - \vec{C}| \geq r \end{cases} \quad (40)$$

Here, the definition of  $f(x)$  is the same as before. In this circular region, the mapping is still perfect.

The above only considers the adjustment of plane coordinates. The thickness coordinate depends on the plane coordinate, and its adjustment can be calculated according to the method of Subsection B.

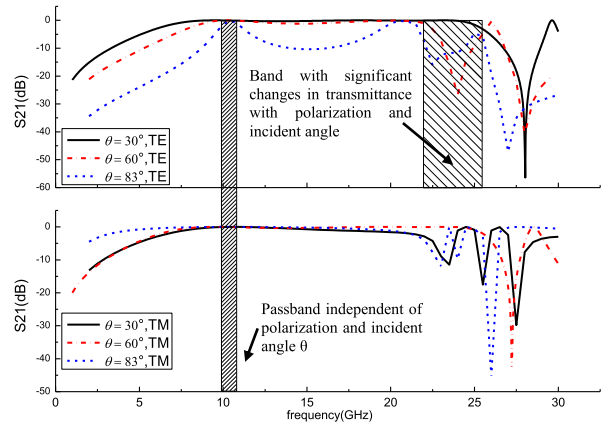


FIGURE 8. The transmission characteristics of the unit-cell at different incident angles.

Fig. 6(a) is the distortion of the grid with a spacing of 0.01 caused by the adjustment of the unit-cell position when  $r = 0.15$  and the maximum position offset  $\vec{d}_{\max} = (0.03, 0.03)$  is taken. Fig.6(b) shows the distortion caused by the element size adjustment to the grid with a spacing of 0.01 when  $\epsilon_{\max} = 0.3$  is applied. In both cases,  $f(x) = (\cos x + 1)/2$  is taken. It can be seen from the figures that the position and shape adjustments of the elements in the affected area are continuous and adjustable in both cases. This local geometry adjustment method can be used as a tool of fine-tuning for arrays and electrical performance optimization for curved FSSs.

#### IV. ACTUAL EFFECT

An example of arranging multilayer hybrid unit-cells on a typical shaped radome is selected to test the effect of this method.

##### A. THE UNIT-CELL FOR ARRANGEMENT

Fig. 7 shows the unit-cell of a three-layer patch-aperture hybrid array. The shape parameters  $L = 4.2$  mm,  $R_0 = 3.4$  mm,  $R_1 = 4$  mm,  $R_2 = 1.8$  mm and  $h = 2.5$  mm. The first layer and the third layer are consisted of conductive wafers, which are used as micro-elements to load the hexagonal-loop apertures in the middle layer. The interlayer between two array layers is filled with low density medium with dielectric constant of 1.04 and loss tangent of 0.001. Fig.8 is the typical frequency response curve of transmission of the unit-cell at different incident angles. The unit-cell has a passband basically independent of polarization and incident angle in the band of 10~11 GHz.

##### B. THE RADOME MODEL FOR TEST

A simplified radome model is selected as an example of electromagnetic functional structure. The shape of the mid-surface of the radome is shown as the yellow surface in Fig.9. The light green area at the tip is no need to arrange unit-cell, and the green sheet at the bottom is an analog antenna

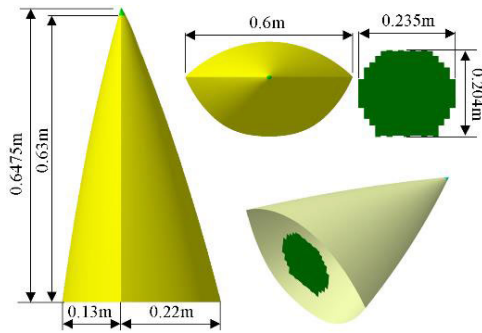


FIGURE 9. The antenna-radome system for test.

panel. The mid-surface of the radome is composed of upper and lower parts, and the cross profile is a helmet shape with low scattering.

C. UNIT-CELL ARRANGEMENT ON THE RADOME

Since the radome is assembled by an upper part and a lower part, there is a natural edge. Near the edge, both the integrity of unit-cells and the continuity of the array are difficult to maintain and unnecessary. Therefore, the upper part and the lower surface can be treated independently.

Because the unit-cell is symmetrical in the thickness direction and has a mid-layer array, the mid-layer of the unit-cell will fit with the unfolding reference surface. The reference surfaces of the upper and lower parts are discretized into triangular facets models with a maximum side length of 3mm near the boundaries and 10mm in other areas, and then flat-unfolded by the minimum distortion method present in Section II with all  $t_j = 1$ . The unfolding results are shown in Fig.10. It can be found that the maximum linear deformation on the reference surface of the lower part is about 1.23% which occurs at the bottom edge and center. The situation on the upper part is similar, but the maximum linear deformation is about 1.13%. If we want the linear distortion in the central area of the reference surfaces of the upper and lower parts to be as small as possible, we can set the weight  $t_j$  of facets in the central area to be greater than 1. As a result, the linear distortion in the most central area decreases, but that at the surface edge increases, with a maximum value of more than 3%. Since the resonant wavelength is usually proportional to the aperture or patch size of the unit-cell, this level of deformation or center wavelength shift is acceptable for broadband FSSs.

As shown in Fig.11, the unit-cells are arranged on the unfolding solution of the reference surface. The starting points of the arrangement are on the symmetry axes of the unfolding solutions. The central positions and local coordinate systems of unit-cells are determined. In order to ensure the integrity of unit-cells near the edges and ensure that elements (especially micro-element patches) are not too close to the boundary and cause adverse effects, a minimum safe distance between unit-cells and the boundary is set as 1.8mm. Fig.11 is a distribution map of unit-cells on

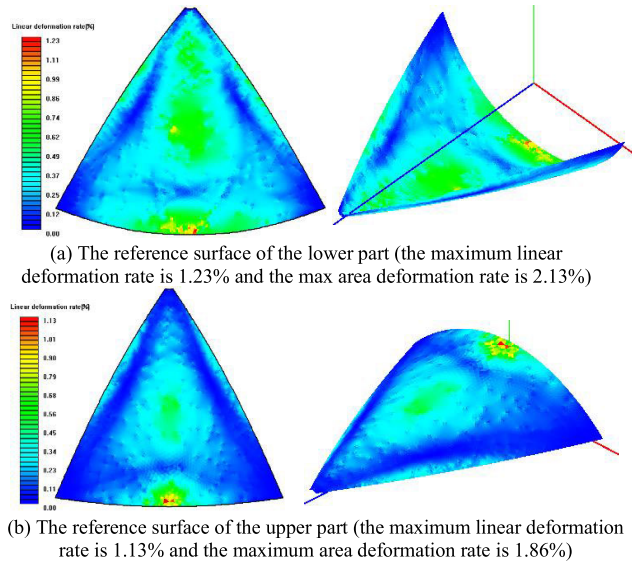


FIGURE 10. Deformation distribution of the mid-surface of the radome after flat unfolding.

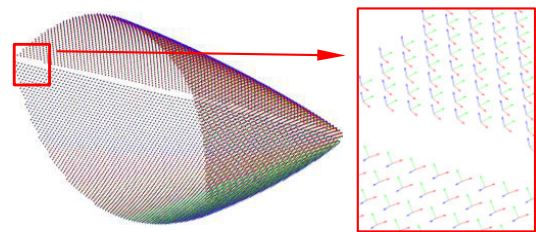


FIGURE 11. Distribution map of unit-cells on the radome. Blue denotes the z-axis of the local coordinate system of each unit-cell (also the normal direction at the center of unit-cell), while red denotes the x-axis.

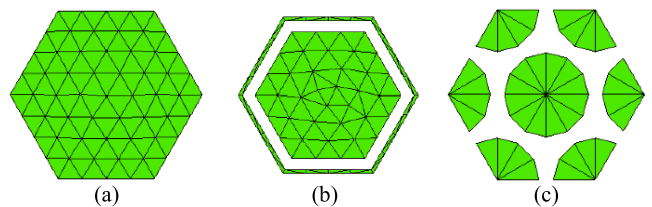


FIGURE 12. Discrete facets of the unit-cell. triangular facet model of a planar period (a), the mid-layer (b) and the micro-element layers (c).

the radome after modeling according to the above method. Each unit-cell is marked with a z-axis vector and an x-axis vector of the local coordinate system of the unit-cell. Among them, 5064 unit-cells are arranged on the upper part and 6208 unit-cells are arranged on the lower part of the radome. For most high-frequency approximate electromagnetic calculation methods, the model shown in Fig.11 is sufficient to meet the input requirements.

According to the method in Section III, first discretize a planar period of the unit-cell into triangular facets as shown in Fig. 12(a) (taking a regular hexagon instead of a parallelogram as the period is to ensure the integrity of the regular hexagon-annular aperture). Then discretize the conductive



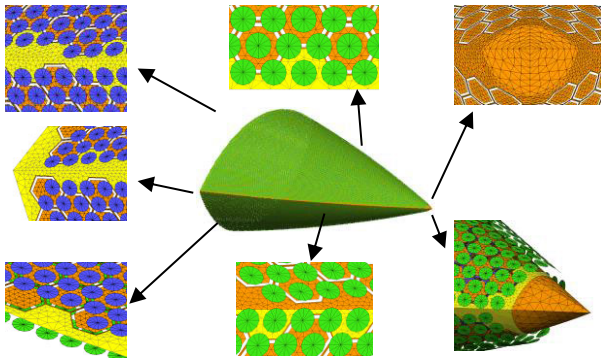


FIGURE 13. The three array layers of the model radome.

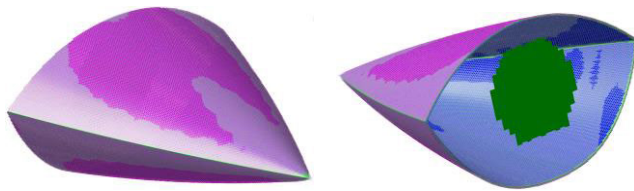


FIGURE 14. The complete model of the FSS radome-antenna system.

regions of the mid-layer and the two micro-element layers into triangular facet models, as shown in Fig. 12(b) and 12(c) respectively. To make it convenient to complement the micro-elements near the boundary into circles, each circular patch is equally divided into 12 triangles according to the central angle.

According to (29) and (30), the representation coefficients of vertices of the facet model of every layer with respect to the vertices of the facet model of the planar period in Fig.12(a) are determined. Then the triangular facet models of the three array layers are obtained by conducting the processes in Section III-B. For the mid-layer, there are still residual regions after unit-cell arranged. Considering it is an aperture array, the residual regions need to be filled into conductive region. The residual regions of the original surface (here is also the unfolding reference surface) can be obtained by cutting the original surface with the residual region boundaries.

The dielectric interlayer between the three array layers can be directly generated by the thickness offset of the mid-surface.

Fig. 13 shows the mesh model of the three array layers after unit-cell arrangement. A conductive surface is set at the tip to ensure the integrity of the mid-layer. It is shown that, although the width of conductive belt between hexagonal-annular apertures is only about 0.34 mm, there is no connection between the adjacent apertures, only a tiny size change. In fact, the size change depends on the linear deformation of the flat-unfolding solution, while the accuracy of topological features depends on the computational accuracy. On the other hand, the two micro-element layers and the mid-layer are also

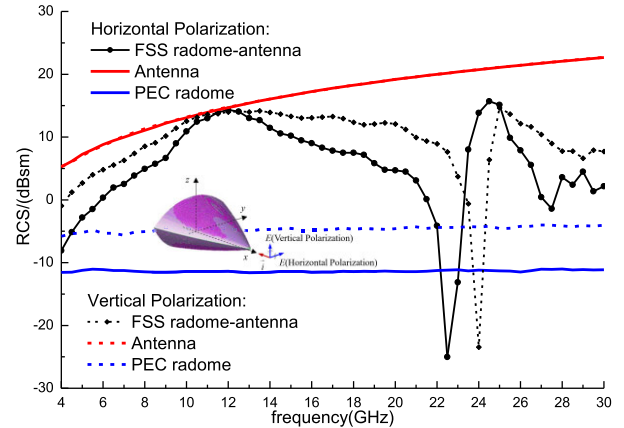


FIGURE 15. Monostatic RCS of the FSS radome-antenna system variation with frequency.

TABLE 1. Comparison to existing methods.

Method	Advantages	Disadvantages	Ref.
Direct flattening methods	Easy to arrange unit-cells, high accuracy.	Only applicable to surfaces with 0 Gaussian curvature.	[3]-[6]
Methods based on approximate developable surface	Simple algorithm and easy modeling.	Accuracy is affected by the approximation and local projection method.	[7][16]
Local tangent plane approximation methods	High local accuracy and easy to conduct, suitable for sparse arrays.	Involving many splicing issues, not suitable for densely arranged arrays.	[8][9][11]
Equal geodesic distance method	Easy to solve regular surfaces, high local accuracy.	Large error for large range arrangement, and other methods are needed to correct the cumulative error of Geodesic direction.	[12]-[18]
Combination of equal density and equal Geodesic distance	Easy to conduct, suitable for sparse arrays.	Difficult to handle tight arrays and complex elements.	[17][18]
Traditional minimum distortion flattening method	Easy to arrange arrays, good topological characteristics.	High computational cost, difficult to control local array deformation, and hard to handle variable thickness situations.	[19]-[21]
This method	Excellent topological characteristics, high precision, easy to handle variable thickness situations.	High computational cost.	

aligned in the normal direction, which demonstrates the advantages of the perfect mapping from the flat-unfolding plane to the original surface.

The complete FSS radome model is obtained by adding the dielectric interlayer to the model shown in Fig.14. A total of  $1.42 \times 10^6$  conductive triangular facets and  $4.04 \times 10^7$  dielectric tetrahedral meshes are finally obtained after meshing.

#### D. THE ELECTROMAGNETIC PERFORMANCE OF THE FSS RADOME-ANTENNA SYSTEM

Fig. 15 shows the calculated result of the monostatic radar cross section (RCS) variation with frequency of the model shown in Fig. 13. For the convenience of comparison, the monostatic RCS of individual antenna and a pure perfect electric conductive (PEC) radome with the same shape as the mid-layer of the FSS radome are given in the same figure. The monostatic RCS of the model in Fig. 15 is calculated by a method of volume integral equation combined with the method of moments (VIE-MOM) and accelerated by the multi-level fast multipole algorithm (MLFMA), while the results of the individual antenna and the pure PEC radome are calculated by MOM-MLFMA. The radiation direction of the electromagnetic wave is along the axis of the radome, and the local incidence angle of the radome surface varies from  $62.7^\circ$  to  $82.8^\circ$ . The results indicate that the RCS of the FSS radome-antenna system is lower than that of the pure antenna in the whole investigation frequency band. The RCS of the FSS radome-antenna system near 10~12GHz is close to the RCS of the antenna, which may be due to that this frequency band is approximately a passband of the unit-cell independent of incident angle and polarization condition. Outside this frequency band, the transmission of the unit-cell is always low in at least one polarization state, resulting in partial blocking of the incident wave and the antenna reflecting wave. In the frequency band around 22.5~24 GHz, the RCS of the FSS radome-antenna system is even lower than that of the pure PEC radome, which may be caused by the low transmission of the FSS radome and the spatial lobes which radiate part of the energy to other directions.

#### V. CONCLUSION

For the above example where a compact array composed of regular hexagonal unit-cells is arranged on an undevelopable surface, existing methods are usually powerless. Using the method presented in this manuscript, a distortion controllable modeling result is presented, and the potential of this modeling result for monostatic RCS calculation of antenna radome systems is demonstrated. This demonstrates the superiority and potential of modeling complex curved array structures based on the minimum distortion flat-unfolding solution of curved surfaces.

Compared with existing methods, the advantages and disadvantages of this method are shown in Tab. 1. The advantages of this method are good topological characteristics and high accuracy of the modeling result, and the ability to handle variable thickness structures, but the cost is relatively large computational complexity.

This method actually provides an algorithm for establishing a perfect mapping between a finite planar periodic structure and the target thick surface. Theoretically, if a 3D unit-cell can be discretized into a mesh model, the geometric information of a periodic array consisting of these unit-cells can be fully mapped to the thick curved surface to form a

discrete mesh model of the curved FSS structure. In this modeling method, the distortion degree of unit-cell and array can be evaluated by the deformation distribution of the flattening solution and the curvature of the reference surface. The deformation of the unit-cell and array on the surface can be controlled not only by the flattening process, but also by the local adjustment of the planar array before mapping, which lays a foundation for the electrical performance optimization of the curved array structure. In addition, this method can also be used as a design scheme representation tool for the electromagnetic functional structure of thick curved surface, providing calculation models for high-frequency and low-frequency algorithms, and providing data sources for digital production.

In fact, the accuracy of this method is directly dependent on the accuracy of the discrete meshes of the reference surface and the unit-cell. Excessively coarse discrete meshes may cause the modeling results to be not smooth enough (unable to approach the contour of the radome well). Improving the smoothness of modeling results by increasing the accuracy of mesh discretization will lead to a surge in computational complexity. If the nodes of the modeling results are calibrated using the original NURBS (Non-Uniform Rational B-Spline) surface representation of the reference surface or the radome contour surface, the accuracy of the modeling results can be greatly improved, making it not limited by the discrete meshes of the reference surface and the unit-cell. The authors' future work will focus on how to carry out the integrated optimization of electromagnetic performance, aerodynamic and structural optimization of curved array structures based on this modeling method.

#### REFERENCES

- [1] Y. X. Li, P. Zhang, and L. Bai, "Research status and challenges on the 3D printing electromagnetic functional structure," *Aeronaut. Sci. Technol.*, vol. 34, no. 8, pp. 1–10, 2023.
- [2] L. X. Yao, "Functional design and realization of electromagnetic tunable structure based on graphene/ion gel," M.S. thesis, School Electron. Sci., Nat. Univ. Defense Technol., Changsha, China, Apr. 2021.
- [3] T. K. Wu, *Frequency Selective Surface and Grid Array*. New York, NY, USA: Wiley, 1995.
- [4] J. C. Vardaxoglou, *Frequency Selective Surfaces Analysis and Design*. New York, NY, USA: Wiley, 1997.
- [5] B. A. Munk, *Finite Antenna Arrays and FSS*. New York, NY, USA: Wiley, 2003.
- [6] H. Zhou, S. Qu, B. Lin, J. Wang, H. Ma, Z. Xu, W. Peng, and P. Bai, "Filter-antenna consisting of conical FSS radome and monopole antenna," *IEEE Trans. Antennas Propag.*, vol. 60, no. 6, pp. 3040–3045, Jun. 2012.
- [7] E. García, C. Delgado, and F. Catedra, "Efficient iterative analysis technique of complex radome antennas based on the characteristic basis function method," *IEEE Trans. Antennas Propag.*, vol. 69, no. 9, pp. 5881–5891, Sep. 2021.
- [8] K. Persson, M. Gustafsson, G. Kristensson, and B. Widenberg, "Source reconstruction by far-field data for imaging of defects in frequency selective radomes," *IEEE Antennas Wireless Propag. Lett.*, vol. 12, pp. 480–483, 2013.
- [9] J. Moreno, M. Fernandez, and A. Somolinos, "Analysis and design of antenna radomes," in *Proc. IEEE Int. Conf. Microw.*, Tel Aviv, Israel, Dec. 2013, pp. 1–5.
- [10] M. Zhu, H. Q. Wang, Z. L. Wang, and G. H. Zong, "Key technology of robot digital machining system for complex FSS," *Aeronaut. Manuf. Technol.*, vol. 1, pp. 61–67, Jan. 2005.

- [11] X. Y. Hou, "A novel frequency selective surfaces patch design for double curved radome," *J. Projectiles, Rockets, Missiles Guid.*, vol. 26, no. 1, pp. 123–125, 2006.
- [12] C. Pelletti, G. Bianconi, R. Mittra, and A. Monorchio, "Analysis of finite conformal frequency selective surfaces via the characteristic basis function method and spectral rotation approaches," *IEEE Antennas Wireless Propag. Lett.*, vol. 12, pp. 1404–1407, 2013.
- [13] C. L. Valle, G. T. Carranza, and R. C. Rumpf, "Conformal frequency selective surfaces for arbitrary curvature," *IEEE Trans. Antennas Propag.*, vol. 71, no. 1, pp. 612–620, Jan. 2023.
- [14] F. Liang and J. Gao, "A novel method for fabricating curved frequency selective surface via 3D printing technology," in *Proc. Int. Symp. Optoelectronic Technol. Appl. Int. Soc. Opt. Photon.*, May 2014, Art. no. 929513.
- [15] B. P. Gao, S. C. Huang, Z. Y. Ren, Y. Chen, and X. F. Wang, "Design and verification of an integrated free-standing thick-screen FSS radome," *IEEE Antennas Wireless Propag. Lett.*, vol. 7, no. 9, pp. 1630–1634, Jul. 2018.
- [16] X. F. Wang, B. P. Gao, Z. Y. Ren, Y. Z. Lin, and Y. Chen, "Integrated curved-surface conformal frequency selective surface radome," *Opt. Precis. Eng.*, vol. 26, no. 6, pp. 1363–1369, 2018.
- [17] J. Zhang, "Research on finite frequency selective surface and its application on radome," Ph.D. dissertation, Univ. Chin. Academy Sci., Beijing, China, 2015.
- [18] X. L. Wei, "Design and laser precision machining technologies for frequency selective surface radome," M.S. thesis, Wenzhou Univ., Wenzhou, China, Mar. 2016.
- [19] W. Jiang, "Approximation algorithms for undevelopable surfaces and its application. Shanghai," M.S. thesis, School Math. Sci., Fudan Univ., Shanghai, China, Apr. 2013.
- [20] A. Qin, "Basic research on laser processing system for functional structure of non-developable surface," M.S. thesis, Dalian Univ. Technol., Dalian, China, Jun. 2022, pp. 31–34.
- [21] M.-Y. Geng, H. Chen, Y. Li, H.-J. He, X.-Z. Bo, X.-L. Yang, Z.-G. Liu, and W.-B. Lu, "Low-cost and stretchable FSS radome based on elastomeric fabric and serpentine mesh layouts," in *IEEE MTT-S Int. Microw. Symp. Dig.*, Nov. 2022, pp. 1–3.
- [22] D. Zhang, J. Li, and J. Wang, "Design patterns of soft products using surface flattening," *J. Comput. Inf. Sci. Eng.*, vol. 18, no. 2, Jun. 2018, Art. no. 021011.
- [23] Y. Zhang and C. C. L. Wang, "WireWarping++: Robust and flexible surface flattening with length control," *IEEE Trans. Autom. Sci. Eng.*, vol. 8, no. 1, pp. 205–215, Jan. 2011.
- [24] G. Chen, L.-S. Zhou, L.-L. An, and K. Zhang, "A novel surface flattening method based on mesh edges," in *Proc. 2nd Int. Conf. Intell. Syst. Design Eng. Appl.*, Sanya, China, Jan. 2012, pp. 129–133.
- [25] G. Zigelman, R. Kimmel, and N. Kiryati, "Texture mapping using surface flattening via multidimensional scaling," *IEEE Trans. Vis. Comput. Graphics*, vol. 8, no. 2, pp. 198–207, 2002.
- [26] L. Saroul, O. Figueiredo, and R. D. Hersch, "Distance preserving flattening of surface sections," *IEEE Trans. Vis. Comput. Graphics*, vol. 12, no. 1, pp. 26–35, Jan. 2006.
- [27] Z. L. Xu, *Elasticity*. Beijing, China: Higher Education Press, 2008.



**HUANG MINJIE** was born in Xiaogan, Hubei, China, in 1982. He received the Ph.D. degree in aircraft design from Beihang University, Beijing, China, in 2008. He is currently an Associate Professor with the School of Aeronautic Science and Engineering, Beihang University. His current research interests include microwave filters and computational electromagnetics.

• • •